Available online at www.sciencedirect.com
ScienceDirect
Trans. Nonferrous Met. Soc. China 35(2025) 2244−2258
Transactions of Nonferrous Metals Society of China
www.tnmsc.cn

Hot processing parameters and microstructure evolution of as-cast Ti−6Cr−5Mo−5V−4Al alloy with millimeter-grade coarse grains

Shi-qi GUO[1], Liang HUANG[1], Chang-min LI[1,2], Heng-jun LUO[2], Wei XIANG[2], Jian-jun LI[1]

1. State Key Laboratory of Materials Processing and Die & Mould Technology, School of Materials Science and Engineering, Huazhong University of Science and Technology, Wuhan 430074, China;
2. China National Erzhong Group Deyang Wanhang Die Forging Co., Ltd., Deyang 618000, China

Received 8 December 2023; accepted 9 April 2024

Abstract: Hot compression experiments were conducted under conditions of deformation temperatures ranging from 950 to 1150 °C, strain rates of 0.001−10 s^{-1}, and deformation degrees ranging from 20% to 80%. The hot deformation behavior and microstructure evolution of millimeter-grade coarse grains (MCGs) in the as-cast Ti−6Cr−5Mo−5V−4Al (Ti-6554) alloy were studied, and a hot processing map was established. Under compression along the rolling direction (RD), continuous dynamic recrystallization (CDRX) ensues due to the progressive rotation of subgrains within the MCGs. Along the transverse direction (TD), discontinuous dynamic recrystallization (DDRX) resulting from grain boundary bulging or bridging, occurs on the boundaries of the MCGs. With decreasing strain rate, increasing temperature, and higher deformation degree, dynamic recrystallization becomes more pronounced, resulting in a reduction in the original average grain size. The optimal processing parameters fall within a temperature range of 1050−1150 °C, a strain rate of 0.01 s^{-1}, and a deformation degree between 40% and 60%.

Key words: as-cast Ti-6554 alloy; millimeter-grade coarse grains; deformation mechanism; hot processing parameters

1 Introduction

High-strength β titanium alloys, comprising metastable β titanium alloy and near-β titanium alloy as the core, exhibit superior mechanical properties [1]. They are currently widely employed in the aerospace industry for large components to meet the design requirements of long life, light-weight and high reliability of flight equipment [2,3]. Proper hot forging processes can effectively enhance the microstructure and properties of titanium alloy components [4]. The processing of millimeter-grade coarse grains (MCGs) is often involved in the forming process of large integral components. For as-cast billets with large grains, techniques such as multi-directional forging [5], upsetting extrusion [6], multi-pass extrusion [7], and multiple rolling [8] are frequently employed in the cogging process to achieve a uniform distribution of equiaxed grains and improved mechanical properties.

Understanding the hot working performance of as-cast titanium alloys, clarifying the deformation mechanism, and determining a reasonable processing window are crucial prerequisites for formulating the cogging process. YANG et al [9] investigated the refinement of Ti−22Al−23Nb−1Zr−1Mo heavy ingots with centimeter-level coarse grains through multi-directional isothermal forging. The results indicated that the alloy can be refined at 1200 °C with 4 passes and 40% reduction. WANG et al [10] explored the hot deformation behavior and the microstructure evolution of as-cast Ti-55511

Corresponding author: Liang HUANG, Tel: +86-13971096516, E-mail: huangliang@hust.edu.cn
https://doi.org/10.1016/S1003-6326(25)66812-9

alloy. They determined the optimal processing window to be within the temperature range of 1000−1050 °C and strain rate range of 0.001−0.01 s^{-1}. In a study by XU et al [11], as-cast TiAl alloys were examined, and a graph with the strain rate sensitivity exponent was plotted to reflect the correlation between process parameters and microstructure evolution. The above research indicates that the selection of temperature, strain rate, and deformation degree is crucial for the grain refinement of as-cast alloys.

The new metastable β titanium alloy, Ti-6554, has exhibited promising comprehensive performance, rendering it suitable for use in large load-bearing aerospace components due to its favorable combination of strength and fracture toughness [12,13]. LI et al [14] elucidated the microstructure evolution of Ti-6554 alloy in the β phase based on power dissipation efficiency. Additionally, LI et al [15] investigated the softening mechanism in the α+β phase region, revealing that the combined effect of dynamic phase transformation and dynamic spheroidization leads to the refinement of α grains. LONG et al [16] proposed extrusion type globularization and cutting type globularization mechanisms to describe the dynamic spheroidization behavior. It is evident that the existing research primarily focuses on forged Ti-6554 alloy with good initial microstructural characteristics. However, the existing results may not be directly applicable to the as-cast Ti-6554 alloy, as the initial microstructure significantly affects the evolution mechanism during hot deformation [17]. Therefore, further research specific to the as-cast Ti-6554 alloy is necessary.

To achieve fine and uniform grains, in this study, hot compression experiments were conducted under various deformation temperatures, strain rates and deformation degrees to generate material flow curves. Subsequently, hot processing maps were established to determine the appropriate processing technology. The microstructure of the deformed specimens was analyzed to fully comprehend the deformation mechanism, which would aid in determining the optimal processing parameters.

2 Experimental

2.1 Materials

The as-cast Ti-6554 alloy billet, with a diameter of 160 mm, was prepared using a vacuum consumable melting furnace. Table 1 provides the specific chemical compositions of the billet. The phase transition temperature of the alloy, determined through metallographic analysis, is measured to be (785±5) °C. Figure 1 illustrates the sampling location of the specimens and the initial microstructure. To ensure uniformity, cylinders with dimensions of d8 mm × 12 mm were cut from a selected half-radius area of the billet. The initial microstructure of the billet consists of a coarse β-grain matrix and fine α-phase. Upon heating the specimens to the single-phase region, only coarse millimeter-grade β grains remain, with the β-columnar crystal size typically ranging from 2 to 5 mm.

Table 1 Specific chemical compositions of as-cast Ti-6554 alloy (wt.%)

Cr	Mo	V	Al	O	Fe	H	N	Ti
6.40	5.44	5.14	3.72	0.19	0.06	0.0008	0.14	Bal.

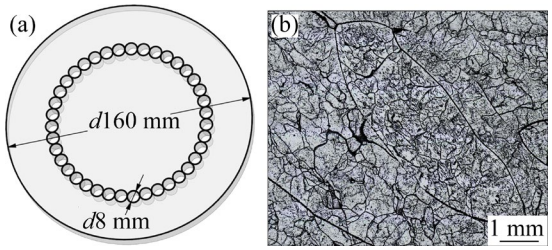

Fig. 1 As-cast Ti-6554 alloy billet: (a) Sampling position; (b) Initial microstructure

2.2 Experimental process

This study aimed to investigate the hot workability and microstructure evolution of the as-cast Ti-6554 alloy using the Gleebe−3500 thermal mechanical simulation testing system. The experimental setup is illustrated in Fig. 2. Initially, the specimens underwent a solid solution treatment at 850 °C for 0.5 h to enter the β phase zone. Subsequently, a platinum−rhodium thermocouple was welded to the specimen surface to enable constant temperature control. To mitigate stress concentration and minimize friction, a lubricant was applied to 0.1 mm-thick tantalum and graphite sheets affixed to the upper and lower surfaces of the cylindrical specimen. Additionally, a vacuum was created in the compression chamber, and argon gas was introduced to maintain a negative pressure environment.

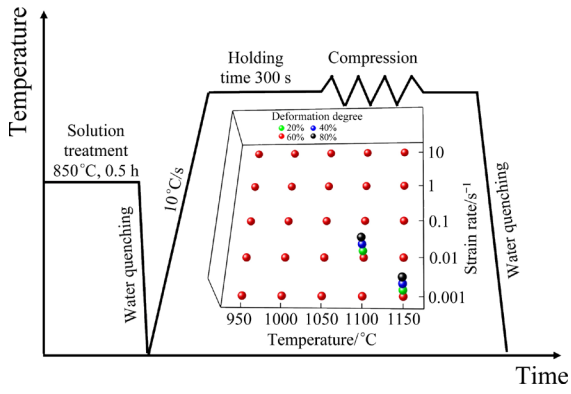

Fig. 2 Experimental diagram of hot compression of as-cast Ti-6554 alloy

The specimen was heated to the target temperature at a rate of 10 °C/s using resistance heating and held for 300 s to ensure uniform microstructure. The working temperature for the as-cast Ti-6554 alloy was chosen to be 150−250 °C above the β transition temperature, as in this range the alloy exhibited optimal plasticity. Figure 2 illustrates specimen preparation and deformation conditions. Uniaxial compression experiments were conducted at five temperatures (T=950, 1000, 1050, 1100 and 1150 °C) and five strain rates ($\dot{\varepsilon}$=0.001, 0.01, 0.1, 1, and 10 s^{-1}). Additionally, two groups of specimens were subjected to different deformation degrees (D=20%, 40%, 60%, and 80%). Immediately after the deformation, the test specimens were quenched with water to preserve the microstructure.

2.3 Microstructural characterization

At the end of the experiment, the specimens were bisected parallel to the compression direction. Following surface polishing, a polishing solution comprising methanol, ethylene glycol, and perchloric acid in a ratio of 7:2:1 was prepared. Subsequently, the surface underwent electro-polishing at 20 V for 15 s using a Buehler electrolytic polisher at room temperature. EBSD observations were then conducted utilizing a GeminiSEM300 field emission scanning electron microscope. Finally, the acquired data were analyzed and processed using OIM analysis software, resulting in outputs such as an inverse pole figure (IPF) map, misorientation distribution, and grain size measurements.

3 Results and discussion

3.1 Stress−strain curves

Figure 3 illustrates the stress−strain curves and their corresponding peak stresses of the as-cast Ti-6554 alloy under different testing conditions. The initiation and interplay of the hardening and

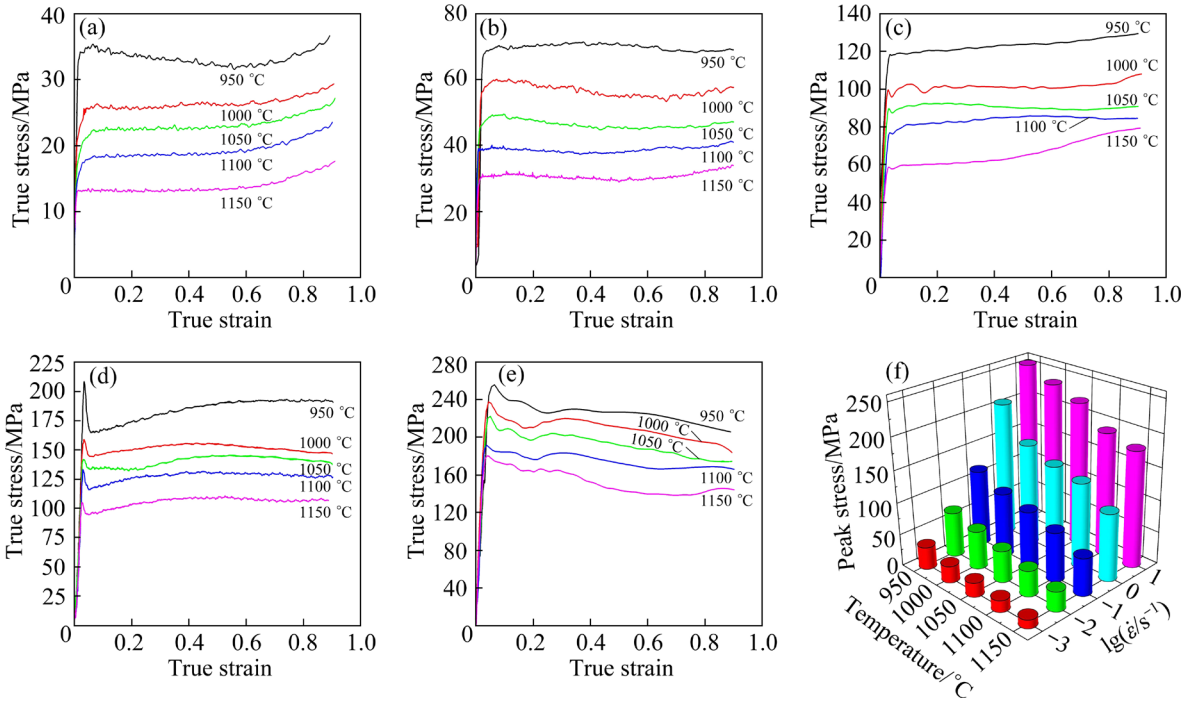

Fig. 3 True stress−strain curves of as-cast Ti-6554 alloy at different strain rates ($\dot{\varepsilon}$) of 0.001 s^{-1} (a), 0.01 s^{-1} (b), 0.1 s^{-1} (c), 1 s^{-1} (d) and 10 s^{-1} (e); Peak stress of as-cast Ti-6554 alloy (f)

softening mechanisms are evident from the variation in flow stress [18]. Initially, during early stages of the deformation, the flow stress sharply increases to a peak value due to the work hardening effect. As the deformation temperature decreases and the strain rate increases, the rate of dislocation proliferation and interaction between dislocations intensifies, resulting in higher peak stress levels [15]. Moreover, the heightened thermal activation at elevated temperatures facilitates dislocations to overcome the pinning effect more readily [14]. Afterward, the flow stress demonstrates various flow behaviors during later stages of deformation.

In contrast to the flow softening typically observed in titanium alloys at lower temperatures [19], the as-cast Ti-6554 alloy deformed with MCGs exhibits a more pronounced work hardening phenomenon. At a strain rate of 0.001 s^{-1}, as the temperature increases, the degree of softening in the stress−strain curves gradually diminishes and shows a slight upturn after reaching a strain of 0.6. This suggests that the intensity of work hardening surpasses that of flow softening during the later stages of processing. The occurrence of dynamic recrystallization (DRX) at lower strain rates can be attributed to flow softening [17]. Conversely, the increase in friction force primarily contributes to the work hardening effect. Throughout the hot compression process, the compression time at a strain rate of 0.001 s^{-1} extends up to 15 min. Consequently, the comprehensive lubrication effect of tantalum sheet, graphite and high-temperature grease gradually diminishes over time.

At a strain rate of 0.01 s^{-1}, the flow stress reaches a peak value before transitions into a steady state, indicating a balance between dynamic softening and work hardening during high-temperature deformation [18]. This phenomenon is commonly observed at higher deformation temperatures, where the deformation mechanism of dynamic recovery (DRV) plays a significant role [20]. At a strain rate of 0.1 s^{-1}, owing to the increase in deformation rate, the work hardening rate induced by dislocations surpasses the softening rate resulting from dislocation annihilation. Consequently, there is a rapid escalation in deformation resistance. At this juncture, the alloy undergoes minimal dynamic recrystallization (DRX), and the softening effect is primarily attributed to DRV.

At the higher strain rates of 1 and 10 s^{-1}, the abrupt decline in stress after reaching the peak is attributed to the discontinuous yielding phenomenon. This occurs due to generation of movable dislocations at the grain boundaries during the initial stage of deformation. These dislocations swiftly accumulate and entangle, progressively spreading into the grain interior with increasing strain, leading to a sharp decrease in flow stress [21]. The serrated oscillation and continuous softening of the flow curve are indicative of material instability, suggesting potential effects of deformation bands (DB) [22] or flow localization (FL) [23]. The low thermal conductivity of titanium hinders the dissipation of heat generated by plastic work during high-rate deformation, resulting in a notable increase in the core temperature of the specimens. This temperature rise promotes atomic activity, facilitating the rearrangement of dislocations into lower-energy configurations, reduction of dislocation density, and enhancement of the softening effect [14]. However, if the local temperature surpasses a reasonable range, it heightens the likelihood of unstable phenomena, which is highly detrimental to material processing.

3.2 Hot processing map

The hot processing map plays a crucial role in uncovering the plastic deformation mechanism and optimizing process parameters, greatly impacting microstructure control [24]. According to the material model proposed by PRASAD et al [25], the deformation process can be viewed as dissipation. The work done by the external load is primarily consumed by plastic deformation and microstructure evolution. The overall power input in the deformation process can be expressed by [26]

$$P=\sigma\dot{\varepsilon}=G+J=\int_0^{\dot{\varepsilon}}\sigma \mathrm{d}\dot{\varepsilon}+\int_0^{\sigma}\dot{\varepsilon}\mathrm{d}\sigma \tag{1}$$

where P is the power absorbed by the alloy, which comprises the power G consumed by plastic processing and the power J related to metallurgical mechanisms; σ is the stress.

The power dissipation efficiency (η) is a dimensionless parameter that reflects the power dissipation of a material. Its physical interpretation is the ratio of the energy dissipated by the microstructure evolution during the material forming process to the linear dissipated energy. A higher value of η indicates greater energy

consumption by microstructure evolution during the deformation process. Conversely, a lower value of η suggests greater energy dissipation through the generation of visco-plastic heat. It is defined as [27]

$$\eta = \frac{J}{J_{\max}} = \frac{2m}{1+m} \tag{2}$$

where $J_{\max}$ is the maximum value of J under ideal dissipation; m denotes the strain rate sensitivity coefficient, which reflects the degree of material softening during hot deformation. It can be described by the following polynomial equation:

$$m = \frac{\mathrm{d}(\lg \sigma)}{\mathrm{d}(\lg \dot{\varepsilon})} = b + 2c\lg \dot{\varepsilon} + 3d(\lg \dot{\varepsilon})^2 \tag{3}$$

The relationship between flow stress and strain rate can be described in logarithmic form using a third-order polynomial, as shown in Eq. (4):

$$\lg \sigma = a + b\lg \dot{\varepsilon} + c(\lg \dot{\varepsilon})^2 + d(\lg \dot{\varepsilon})^3 \tag{4}$$

where a, b, c and d are material constants. Based on the maximum entropy generation principle [28], the plastic flow instability map can be calculated. The instability region of the material can be determined according to the rheological instability criterion:

$$\xi(\dot{\varepsilon}) = \frac{\partial \lg(m/m+1)}{\partial \lg \dot{\varepsilon}} + m \le 0 \tag{5}$$

The parameter $\xi(\dot{\varepsilon})$ represents the instability value determined by deformation temperature and strain rate. On a two-dimensional plane composed of strain rate and deformation temperature, the region with values less than zero denotes the rheological instability region. When determining the process of deformation, it is advisable to avoid using deformation parameters corresponding to unstable areas.

Figure 4 demonstrates that by overlaying the rheological instability region onto the power dissipation maps, we can derive the hot processing maps of the as-cast Ti-6554 alloy under different strains. The colored contour lines in Fig. 4 represent the value of η, while the blue shaded areas depict the instability region. The occurrence of the unstable region and lower power dissipation efficiency simultaneously manifests in the strain rate range greater than 0.1 s^{-1}, primarily influenced by deformation defects such as the adiabatic shear bands or local plastic flow [29]. Initially, during early stages of the deformation, the unstable region

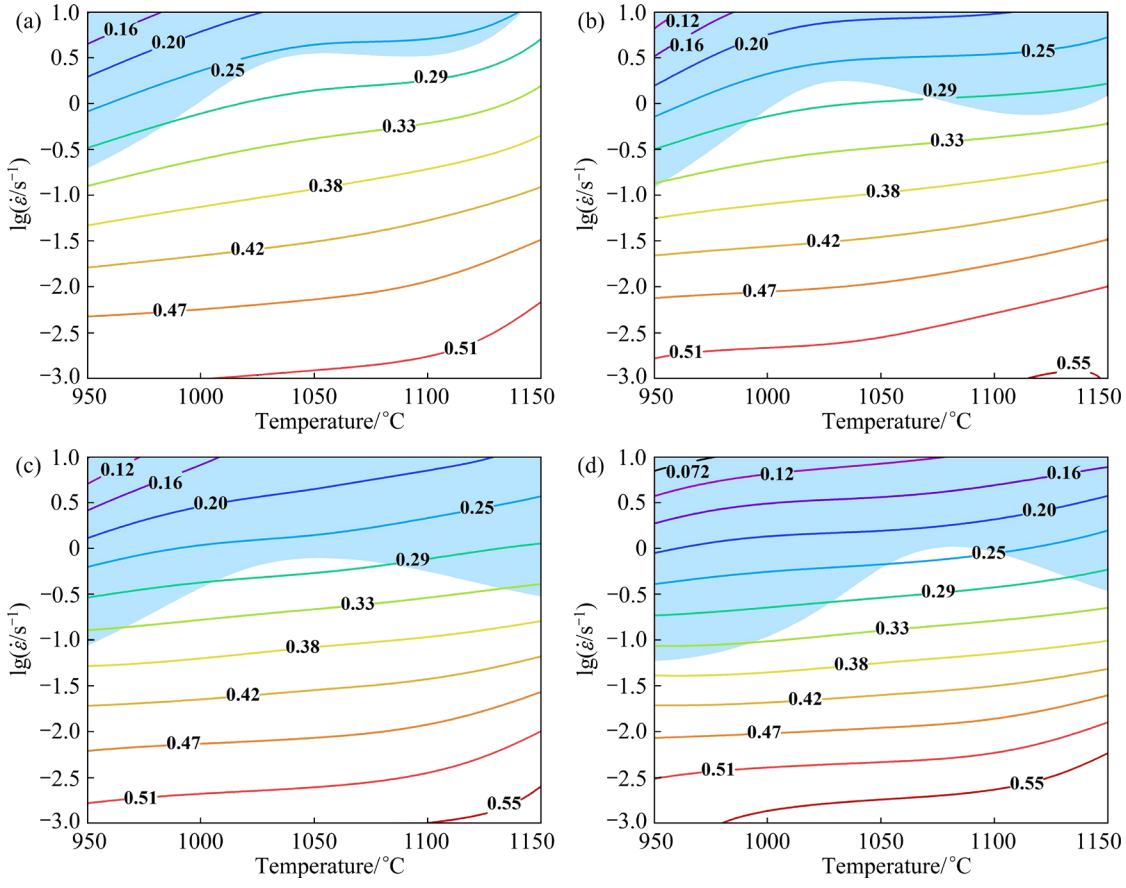

Fig. 4 Hot processing maps of as-cast Ti-6554 alloy at strain (ε) of 0.3 (a), 0.5 (b), 0.7 (c) and 0.9 (d)

appears relatively small. However, as the strain increases from 0.3 to 0.9, the shaded areas expand to 17.1%, 27.2%, 34.4% and 37.7%, respectively. This indicates a gradual expansion of the instability zone with increasing strain. The phenomenon of instability is more pronounced at lower temperatures. Additionally, the power dissipation efficiency increases with the rise of deformation temperature, with the peak value corresponding to the low strain rate region.

3.3 Microstructure

3.3.1 Effect of deformation temperature on microstructure evolution

In determining the deformation mechanism, relying solely on stress−strain curves and hot processing maps may not provide accurate results. Therefore, conducting in-depth research on microstructure becomes essential. Figure 5 presents the IPF maps, misorientation distribution, and the size and quantity of β grains at various deformation temperatures. The misorientation angles ranging between 2° and 10° are considered as low-angle grain boundaries (LAGBs), represented by the white line, while angles exceeding 10° are categorized as high-angle grain boundaries (HAGBs), represented by the black line. In Figs. 5(e, f), D_{all} denotes the average diameter of all grains, D_d represents the average grain size of the newly generated recrystallized grains, and D_m is defined as the average grain size of the matrix MCGs.

The three specimens studied were selected under high temperatures (1000−1100 °C) and low strain rates (0.001 s^{-1}). Under these conditions, all values of η exceed 0.55, indicating that this high power dissipation area constitutes a safe processing zone [30]. Figure 5(a) illustrates a significant DRX phenomenon observed among large columnar crystals at 1000 °C. The original MCGs are elongated. Although a considerable number of LAGBs (77.4%) provide a foundation for the generation of DRX, its development is restricted by low deformation temperatures, resulting in an uneven distribution of grain sizes.

With a further increase in temperature to 1050 and 1100 °C, the extent of DRX in the β phase notably intensifies, characterized by a higher quantity and greater expansion of grains (Figs. 5(b, c)). Combination of high deformation temperatures and low strain rates offers ample energy and duration for microstructure evolution. From Fig. 5(d), the proportion of LAGBs decreases to 72.4% at 1050 °C and 63.1% at 1100 °C, indicating a transition from LAGBs to HAGBs with increasing deformation temperature. Consequently,

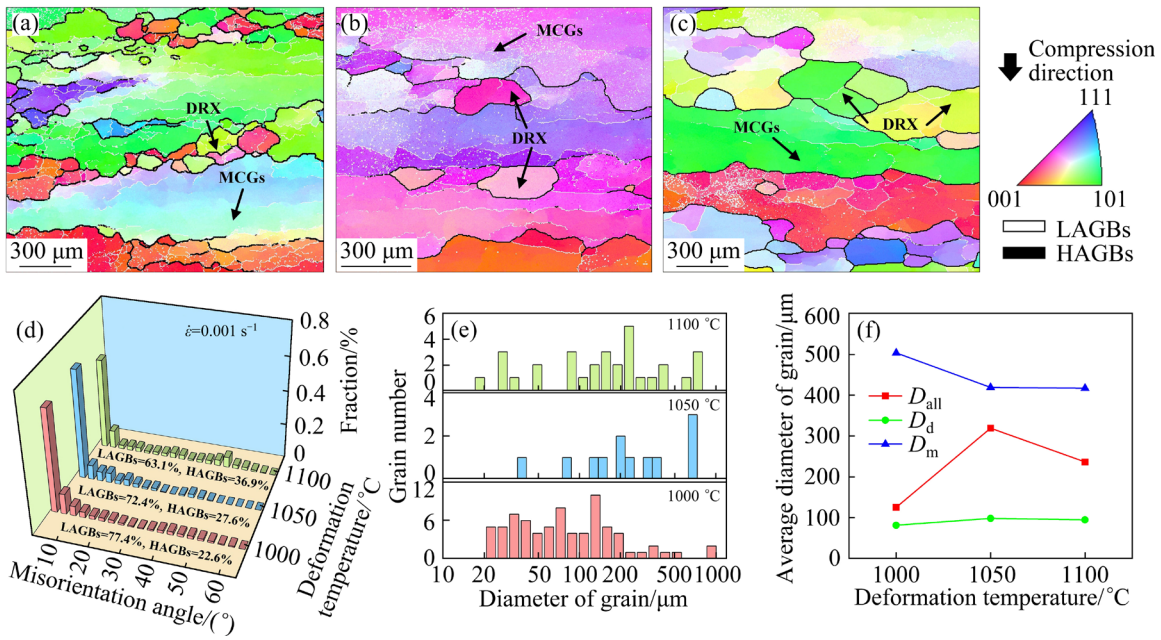

Fig. 5 IPF maps of as-cast Ti-6554 alloy at $\dot{\varepsilon}$=0.001 s^{-1}, D=60% and different temperatures of 1000 °C (a), 1050 °C (b) and 1100 °C (c); Misorientation distribution (d); Number of grains of different diameters (e); Average diameter of grains (f)

statistical data reveal an increase in D_d from 81.6 to 98.5 μm and a decrease in D_m from 502.8 to 416.9 μm. The size of DRX grains enlarges, while the number of DRX grains diminishes, ultimately leading to the refinement of the original MCGs.

3.3.2 Effect of deformation degree on microstructure evolution

Figure 6 illustrates the impact of deformation degree on microstructure evolution at 1150 °C and 0.001 s^{-1}. At a deformation degree of 20%, the active DRV process generates numerous LAGBs, accounting for 75.0% of the microstructure (Fig. 6(a)). Additionally, prominent recrystallized grains are observed at the intersections of grain boundaries in three MCGs. The average diameter D_d measures 75.2 μm, while D_m is recorded at 746.9 μm.

As the deformation degree increases to 40% (Fig. 6(b)), the proportion of LAGBs rises to 78.6%. However, with further increases in the deformation degree to 60% and 80%, the proportion of LAGBs rapidly declines to 59.4% and 50.9%, respectively. During the initial stage of deformation, the dislocation density tends to rise sharply, facilitating the accumulation of LAGBs. Subsequent larger deformations result in higher storage energy and longer durations, creating a conducive environment for the nucleation and growth of the DRX, consequently consuming a certain amount of LAGBs.

At a deformation degree of 60% (Fig. 6(c)), the DRX becomes predominant, resulting in significantly refined grains, with an average diameter (D_d) of 65.2 μm and D_m of 463.2 μm. At this juncture, the value of η reaches its peak dissipation efficiency of 0.6. When the deformation degree escalates to 80%, nearly all the grains (Fig. 6(d)) undergo recrystallization. However, owing to the prolonged duration of isothermal deformation, the DRX grains exhibit substantial growth, with D_d measuring 150.3 μm and D_m at 328.8 μm. Interestingly, a few small secondary DRX grains with an average diameter of 23.3 μm emerge at the primary cluster of DRX grain boundaries. This observation suggests that DRX does not always lead to coarsening, and there exists a critical state that triggers the nucleation and growth of a new generation of DRX.

The findings in this section shed light on the impact of slightly higher strain rates on microstructure evolution at 1100 °C and 0.01 s^{-1}. At a deformation degree of 20%, the average grain diameter (D_m) is 746.4 μm. The presence of serrated boundaries and raised interfaces suggests a deficiency in deformation storage energy, resulting in only precursors of DRX grain nucleation [31]. As the deformation increases to 40%, the proportion of LAGBs rises from 68.8% to 73.3%, indicating the predominance of the DRV mechanism. Additionally, fine grains and subgrains emerge between two large coarse grains, and the formation of recrystallized grains initiates.

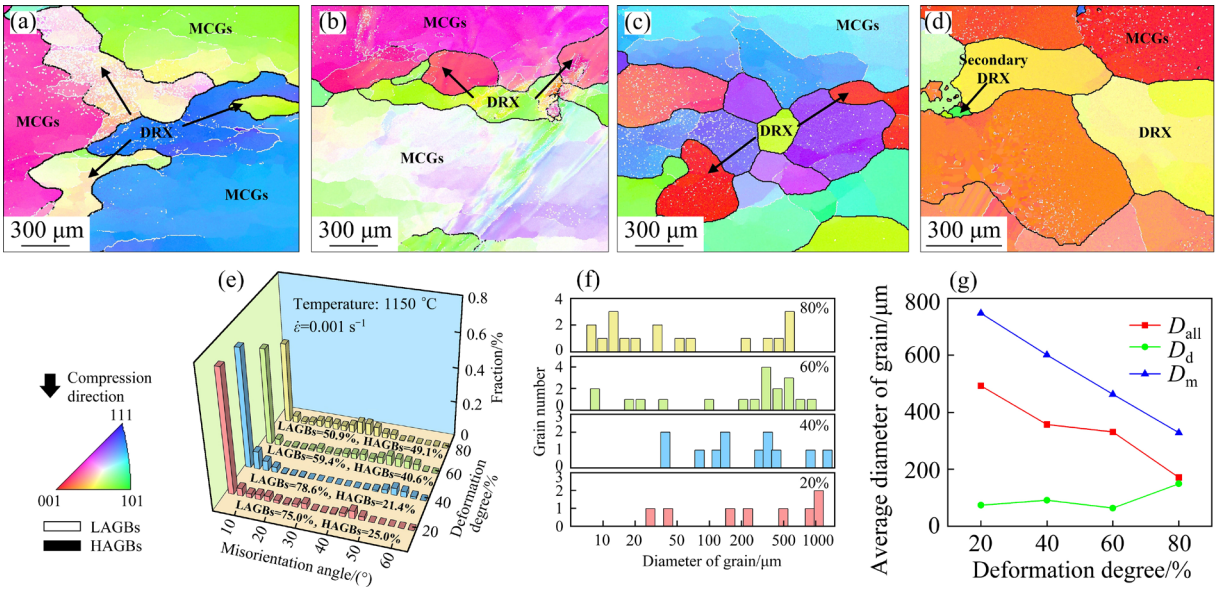

Fig. 6 IPF maps of as-cast Ti-6554 alloy at $\dot{\varepsilon}$=0.001 s^{-1}, T=1150 °C and different deformation degrees of 20% (a), 40% (b), 60% (c) and 80% (d); Misorientation distribution (e); Number of grains of different diameters (f); Average diameter of grains (g)

When continuing to increase the deformation degree to 60% and 80%, the occurrence of DRX significantly improves. The proportion of LAGBs decreases to 65.0% and 59.3%, respectively. Simultaneously, the average grain diameter (D_m) decreases from 576.2 to 339.5 μm, while the average grain diameter of recrystallized grains (D_d) increases from 42.2 to 56.5 μm. The dissipation efficiency value in Fig. 7(c) is 0.47. At deformation degree of 80%, the DRX grains extend into uniform layered coarse grains along the strip, as depicted in Fig. 7(d). However, compared to the complete recrystallization observed in Fig. 6(d), there are still many MCGs that remain effectively unrefined, resulting in an unsatisfactory microstructure distribution. This is attributed to the predominant uniaxial stress state under the unidirectional compression, leading to the stretching of MCGs. To mitigate structural inhomogeneity, various approaches such as different loading directions and multiple processing passes are commonly employed under different deformation degrees [32]. These techniques aim to achieve equiaxed crystals and enhance mechanical properties.

From the analysis of the two aforementioned working conditions, it is clear that the original grain size can be effectively reduced with increasing deformation due to the occurrence of DRX. However, it's crucial to acknowledge that DRX grains may undergo further coarsening with higher processing temperature and prolonged deformation time. Additionally, layered elongated crystals are more likely to appear under high deformation degrees. To achieve a forging bar with a uniform structure and optimal performance, it's imperative to meticulously control the deformation strain rate and degree in each reduction pass at a temperature that facilitates recrystallization.

3.3.3 Effect of strain rate on microstructure evolution

Examining the microstructure under high strain rates can offer a more comprehensive description of the alloy. Figure 8 illustrates the impact of different strain rates at 1150 °C and a deformation degree of 60%. As observed in previous sections, DRX occurs within the temperature range of 1100−1150 °C and low strain rates ranging from 0.001 to 0.01 s^{-1}, which optimizes the microstructure. However, higher strain rates do not lead to an increase in DRX levels. Instead, they have adverse effects [15].

Referring to the hot processing map (Fig. 4), the processing conditions at strain rates of 0.1−10 s^{-1} are predominantly within the instability zone, characterized by power dissipation efficiency (η) values of 0.36, 0.26, and 0.14, respectively. Figure 8(a) displays significant amounts of unrecrystallized MCGs. The primary mechanism within these large grains is DRV, with LAGBs accounting for 71.3% of the total grain boundaries.

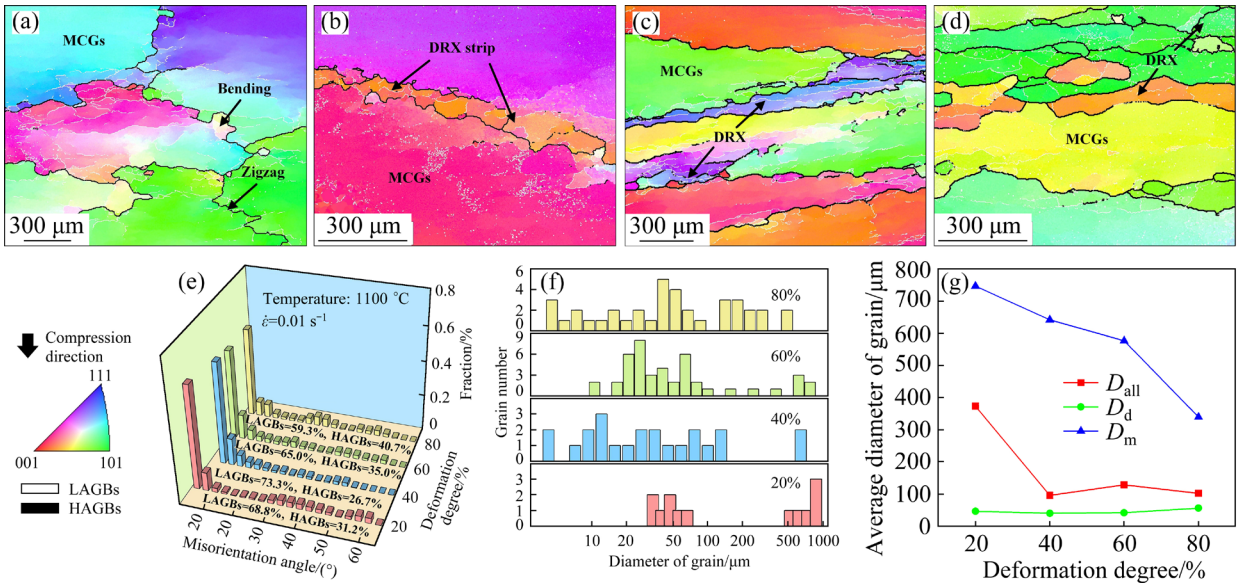

Fig. 7 IPF maps of as-cast Ti-6554 alloy at $\dot{\varepsilon}$=0.01 s^{-1}, T=1100 °C and different deformation degrees of 20% (a), 40% (b), 60% (c) and 80% (d); Misorientation distribution (e); Number of grains of different diameters (f); Average diameter of grains (g)

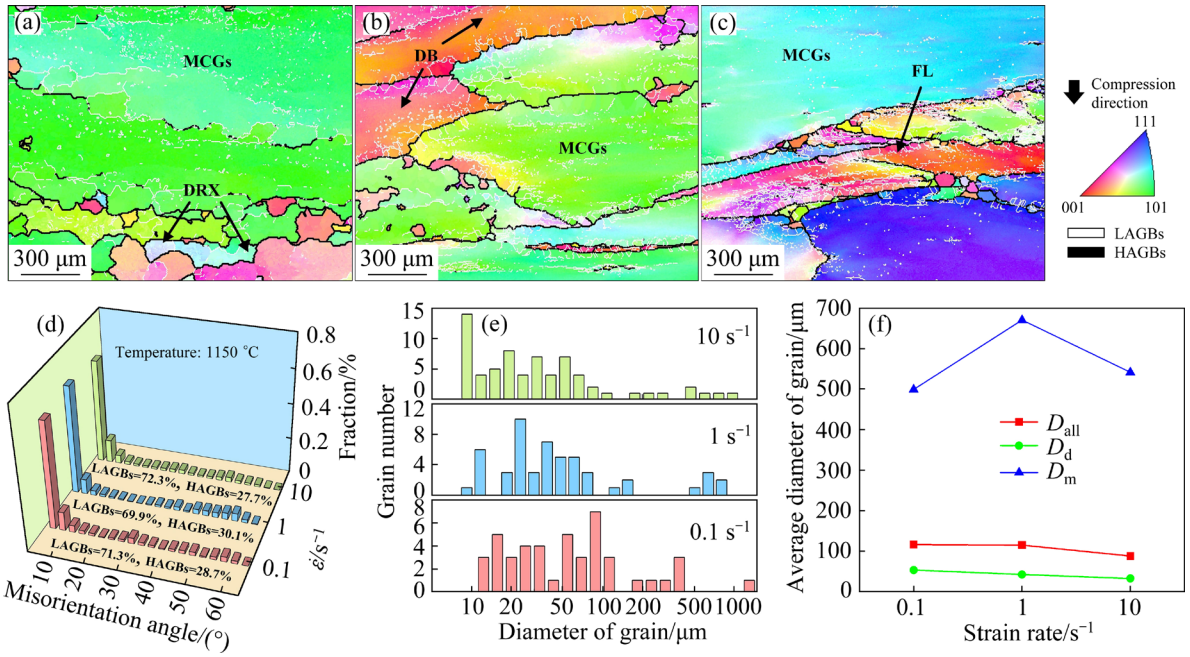

Fig. 8 IPF maps of as-cast Ti-6554 alloy at T=1150 °C, D=60% and different strain rates of 0.1 s^{-1} (a), 1 s^{-1} (b), 10 s^{-1} (c); Misorientation distribution (d); Number of grains of different diameters (e); Average diameter of grains (f)

Fragmented DRX can be noticed at the edge of the IPF map, displaying an uneven tissue distribution. In Fig. 8(b), under a strain rate of 1 s^{-1}, the grains undergo flattening, resulting in the formation of deformation bands (DB) in MCGs that incline approximately 30° from the compression direction [22]. The original coarse grain diameter (D_m) increases from 498.8 to 670.2 μm. At this juncture, minimal DRX grains are formed. This is attributed to the short deformation time at high strain rates, hindering DRX nucleation due to the rapid establishment of a robust dislocation network [33].

In Fig. 8(c), a substantial quantity of LAGBs (72.3%) accumulates near the grain boundary deformation band, indicative of a FL phenomenon [34]. The low thermal conductivity of titanium alloy delays heat dissipation, resulting in deformation instability and irreparable heterogeneous tissue. This localized temperature rise during deformation leads to a rapid decline in flow stress (Fig. 3(e)). In essence, even at a high temperature of 1150 °C, minimal DRX occurs in the instability and low power dissipation efficiency region, rendering it more challenging to refine the grain structure at lower temperatures. Moreover, the localized temperature rises during high strain rate deformation can induce defects such as unstable plastic flow, which must be mitigated when formulating processing conditions for the as-cast Ti-6554 alloy.

3.3.4 Dynamic recrystallization mechanism

CDRX and DDRX are two prevalent softening mechanisms observed in the single-phase microstructure of Ti-6554 alloy during hot deformation [17]. Among these mechanisms, the CDRX facilitates the absorption of dislocations and subgrains through LAGBs, leading to an increase in misorientation and the eventual formation of HAGBs. The gradual rotation of subgrains induces discernible misorientation gradients from the center to the edge of the original grains [35]. This phenomenon primarily occurs within the original grain, with minimal interface migration, resulting in a relatively uniform structural transformation. The onset of CDRX is identified through the accumulation of misorientations exceeding 10°.

IPF maps at a deformation temperature of 1000 °C with strain rate of 0.001 s^{-1}, and a deformation temperature of 1100 °C with strain rate of 0.01 s^{-1} are depicted in Figs. 9(a) and 9(d), respectively. In Fig. 9(b), the cumulative misorientation (point-to-origin misorientation) from A to B is 22.5°, indicating active progressive rotation. The misorientation angles in Fig. 9(e) display a horizontal step change, indicating stability within their respective particles. Figures 9(c, f) illustrate

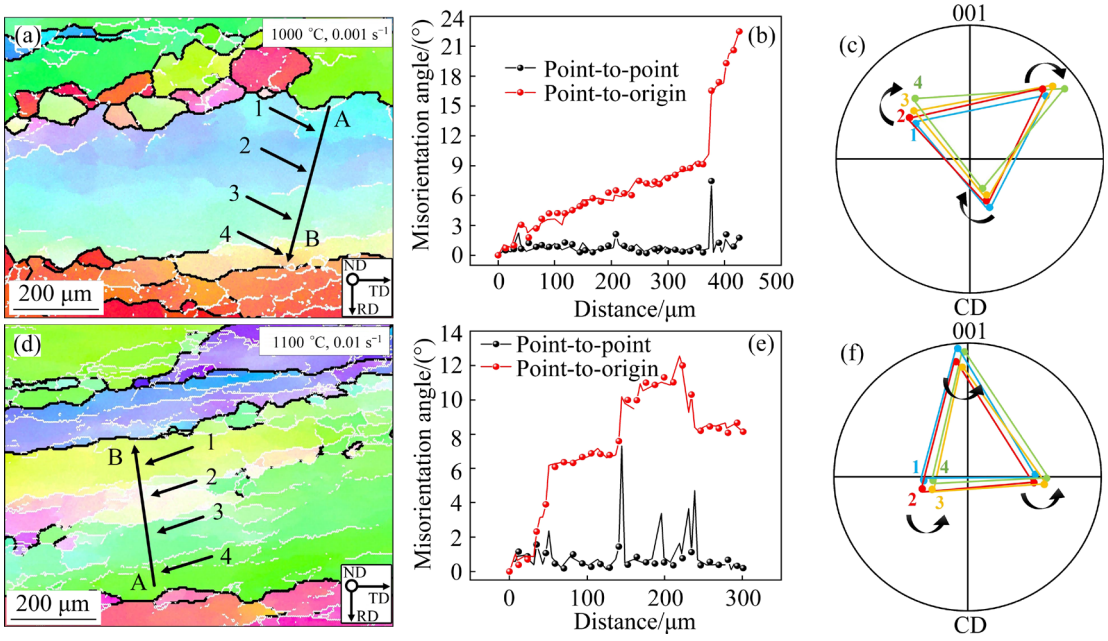

Fig. 9 CDRX mechanism of as-cast Ti-6554 alloy at T=1000 °C, $\dot{\varepsilon}$=0.001 s^{-1} (a–c) and T=1100 °C, $\dot{\varepsilon}$=0.01 s^{-1} (d–f): (a, d) IPF map; (b, e) Misorientation angle along Arrow AB; (c, f) {001} pole figure of marked subgrains

the {001} pole figure between the four subgrains marked in Figs. 9(a, d). The black arrow denotes the direction of rotation of Subgrains 1 to 4. The projection points in Fig. 9(c) rotate clockwise, with point-to-point misorientations of 2.8°, 4.3°, and 10.1°. Conversely, the projection points in Fig. 9(f) rotate counterclockwise, with point-to- point misorientations of 5.9°, 8.0°, and 7.9°. This analysis indicates a gradual increase in cumulative orientation within large grains, accompanied by progressive lattice rotation. Ultimately, the onset of CDRX is characterized by the emergence of fine grains with HAGBs near the grain boundaries of MCGs [36].

DDRX refers to the incubation, nucleation, and subsequent growth of undistorted new grains in deformed tissues. Nucleation typically initiates through grain boundary bow-out, resulting in amorphous grains characterized by evident serrations and bulges [37]. The growth process involves the strain-induced migration of large-angle grain boundaries [38]. In Figs. 10(a, d), IPF maps are presented at a strain rate of 0.001 s^{-1} and deformation temperatures of 1100 and 1150 °C. At this low strain rate, an adequate incubation period facilitates nucleation, leading to a higher volume fraction of DRX and substantial grain coarsening. As observed in Figs. 10(b, e), the cumulative misorientation from A to B is well below 10°, with a relatively minor difference in point-to-point misorientation.

Figure 10(c) displays the {111} pole figure of Grains 1−5 identified in Fig. 10(a), while Fig. 10(f) depicts the {001} pole figure of Grains 1−6 marked in Fig. 10(d). Neither figure reveals a noticeable gradual subgrain rotation process, indicating a random distribution of grain orientations. The migration and expansion of HAGBs absorb dislocations and LAGBs during deformation, indicative of the DDRX deformation mechanism [39]. Additionally, the presence of bridging LAGBs following grain boundary expansion, as indicated by the red arrow, is a characteristic feature of DDRX [40]. As a result of DDRX activity, the formation of new grains and the growth of existing ones occur concurrently during the deformation process. This leads to discrepancies in size between initially formed DRX grains and those formed later, contributing to an uneven microstructure.

From the preceding analysis, it's intriguing to observe that the growth of CDRX grains predominantly aligns with the compression direction of RD, with their evolution primarily occurring within the MCGs. Conversely, the growth of DDRX grains is primarily oriented parallel to the TD and nucleates at the grain boundary of MCGs.

This phenomenon was also reported by CHEN et al [41] in their investigation of Ti-7333 alloy. DDRX primarily facilitates DRX at grain boundaries, whereas CDRX predominantly occurs within grains themselves.

Figure 11 schematically illustrates the microstructure evolution of as-cast Ti-6554 coarse grains during hot working. In the diagram, uncolored regions represent MCGs, red lines denote LAGBs, black lines represent HAGBs, cubes signify subgrain orientation, bending arrows indicate CDRX mechanism, and straight arrows represent DDRX mechanism. Initially, the microstructure appears as a trifurcation of MCGs with sparse dislocation distribution (Fig. 11(a)). During the early deformation stage, DRV predominates, leading to dislocation multiplication. These dislocations undergo reorganization into LAGBs and form a substructure. Concurrently, original HAGBs commence migration and develop jagged bulges (Fig. 11(b)).

As deformation progresses, LAGBs gradually increase their misorientations due to progressive lattice rotations and dislocation accumulations, ultimately forming new HAGBs through CDRX. In the case of DDRX, the nucleation site is characterized by serrated grain boundaries. A few small DRX particles emerge at the intersection of three MCGs and evolve into strips over time. Additionally, there is a phenomenon wherein bridging LAGBs facilitate the formation of new grains after grain boundary expansion (Fig. 11(c)). Due to the considerable size of MCGs, CDRX and DDRX tend to operate concurrently. DDRX primarily stimulates grain boundary migration and nucleation, while CDRX initiates grains subdivision

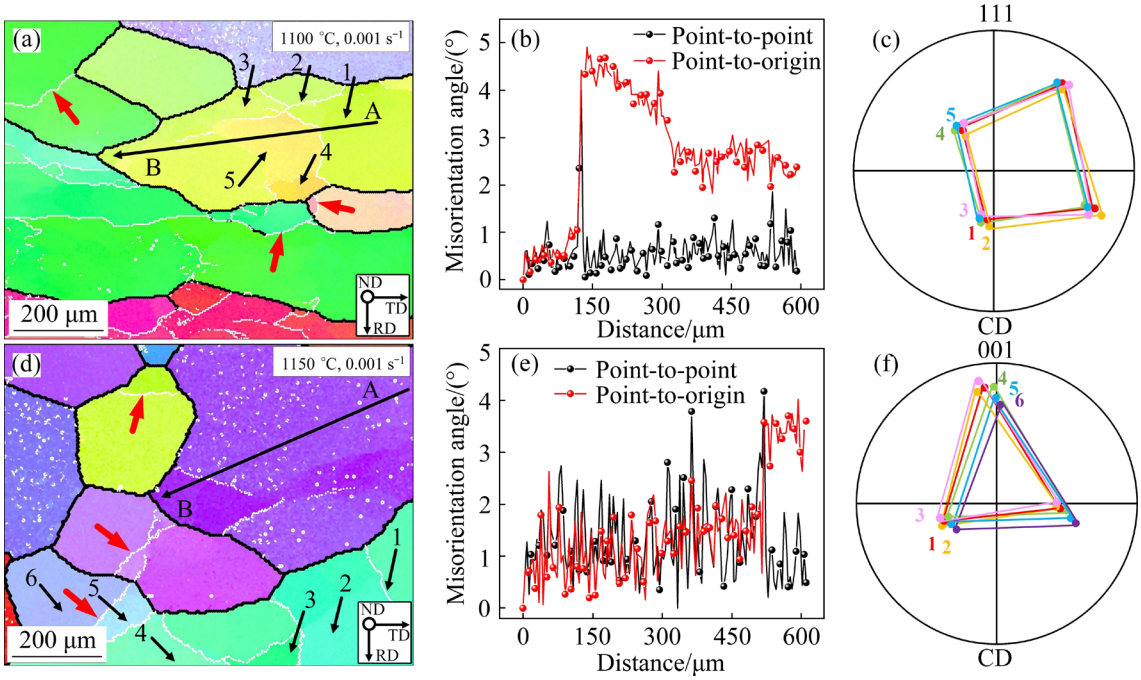

Fig. 10 DDRX mechanism of as-cast Ti-6554 alloy at T=1100 °C, $\dot{\varepsilon}$=0.001 s^{-1} (a–c) and T=1150 °C, $\dot{\varepsilon}$=0.001 s^{-1} (d–f): (a, d) IPF map; (b, e) Misorientation angle along Arrow AB; (c, f) {111} and {001} pole figure of marked subgrains

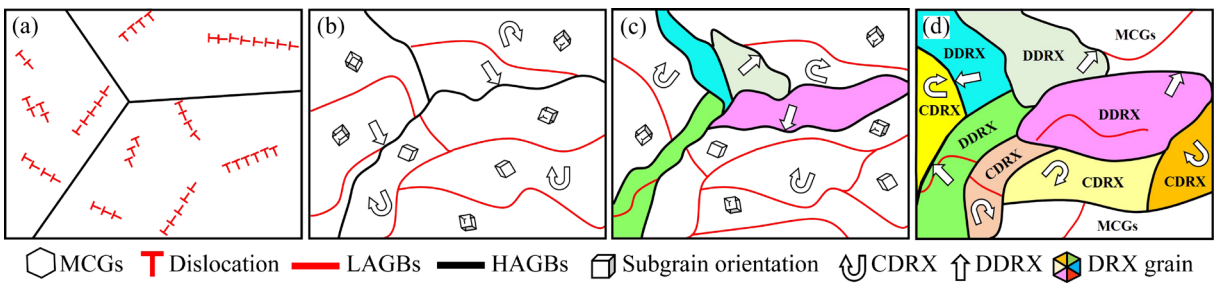

Fig. 11 Microstructure evolution mechanism of as-cast Ti-6554 alloy: (a) Original grain; (b) DRV stage; (c) Initial DRX stage; (d) DRX growth stage

from inside. Towards the end of deformation, under high-temperature and low-strain rate conditions, DDRX can fully proceed. During this phase, dislocation density and LAGBs significantly diminish, and stored energy is released, resulting in enhanced softening effects, substantial grain refinement, and much smoother grain boundaries in the newly generated grains (Fig. 11(d)).

3.3.5 Processing window

The objective of MCGs processing is to partition coarse grains and gradually transform them into equiaxed grains. By considering both power dissipation efficiency and comprehensive microstructure observations, the deformation mechanism of as-cast Ti-6554 alloy can be discerned to establish a rational processing window, as depicted in Fig. 12. Region I, characterized by high strain rates, falls within the instability region (Fig. 8(c)), rendering the alloy susceptible to FL. The η value is lower than 0.21, indicating material instability, necessitating avoidance of this interval. In Region II, the predominant deformation mechanism is mainly DB (Fig. 8(b)). The η value ranges between 0.21 and 0.32. The material remains within the instability zone, with grains experiencing localized or complete elongation.

Region III comprises the instability region characterized by a medium strain rate and low temperature, where $0.26 < \eta < 0.41$. This interval indicates the destabilization observed in Region II and is typified by elongated columnar grains. In Region IV, the η value is between 0.30 and 0.45. Higher temperatures provide more sufficient activation energy. Alongside ongoing DRV, numerous DDRX grains emerge at the interface of the original MCGs (Fig. 8(a)). This phenomenon is more prevalent near the original small grains, resulting in an exceptionally uneven microstructure. Furthermore, due to the short deformation time, CDRX is challenging to occur within MCGs [42].

In Region V, the η value falls between 0.39 and 0.57. At a strain rate of 0.01 s^{-1}, the primary deformation mechanism of the material remains DRV. As nucleation sites for DDRX begin to incubate, the grain boundaries become less distinct. This indicates that the lower temperature and deformation time are still inadequate to induce complete DRX and grain refinement. In instances of minimal deformation (Fig. 7(a)), the grain boundary exhibits a conspicuous zigzag pattern, offering nucleation sites for DDRX. MCGs harbor numerous subgrains, providing ample opportunities for transformation through CDRX. At a strain rate of 0.001 s^{-1}, power efficiency is further enhanced. The deformation mechanism becomes more intricate, with DRV, DDRX, and CDRX occurring concurrently (Figs. 5(a), 6(a) and 7(b)). Notably, CDRX grains predominantly develop along the RD compression direction, while the DDRX grains mainly propagate along the original grain boundaries in the TD, characterized by their relatively flat and fine nature.

In Region VI, the η values range between 0.41 and 0.58. At a strain rate of 0.01 s^{-1}, the deformation mechanisms of DDRX and CDRX are intertwined. Moreover, at higher temperature the

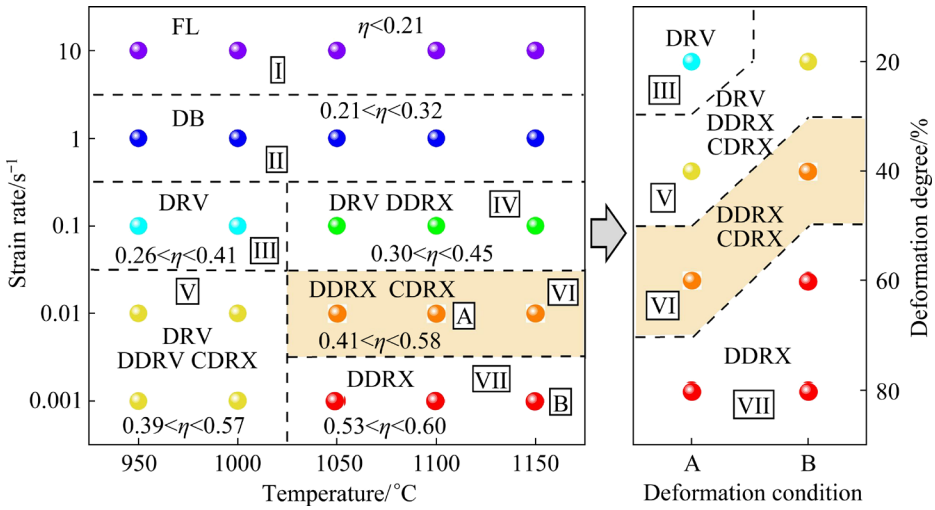

Fig. 12 Deformation mechanism and appropriate processing window of as-cast Ti-6554 alloy under all deformation conditions

growth of DRX grains is significantly enhanced (Fig. 6(b) and 7(c)), which is conducive to the formation of equiaxed grains and represents the most favorable processing interval. However, when the deformation degree reaches 60% or even 80%, the grains align into long strips (Fig. 7(d)), and the structure becomes disordered, indicating that the deformation degree should not be excessively large.

Region VII shows the highest power efficiency, characterized by $0.53 < \eta < 0.60$. Under these conditions, DDRX holds a distinct advantage. At a strain rate of 0.001 s^{-1}, DRX benefits from ample grain boundary migration time. During the migration of subgrains along HAGBs, adjacent dislocations are continually absorbed [43]. Although this condition fosters the formation of more equiaxed grains and reduces the average grain size of MCGs with increasing temperature (Figs. 5(b, c) and 6(c)), prolonged processing time leads to significant coarsening of DRX grains, detracting from structural homogenization. Hence, processing within the lowest strain rate range should be avoided. Ultimately, the yellow shadow region depicted in Fig. 12 emerges as the optimal window for processing as-cast Ti-6554 alloy. The temperature range spans from 1050 to 1150 °C, with a strain rate of 0.01 s^{-1}. In the case of multiple passes, each pass should target a deformation degree falling between 40% and 60%.

4 Conclusions

(1) The instability mechanisms in as-cast Ti-6554 alloy are pronounced at high strain rates, with the instability zone expanding alongside increasing strain. At low temperatures, this instability exacerbates. At moderate strain rates, DRV predominates, while at low strain rates, power dissipation peaks, and DRX becomes active.

(2) The size of MCGs diminishes with decreasing strain rate and rising temperature and deformation degree. DRX grains exhibit gradual growth, promoting a more uniformly distributed microstructure. CDRX occurs along the compression direction of RD, characterized by the progressive rotation of subgrains within MCGs. Along the TD direction, DDRX emerges due to grain boundary bulging or bridging at the boundaries of MCGs.

(3) Excessive deformation degrees coupled with low strain rate can lead to undue grain elongation or significant coarsening, which should be avoided. The recommended processing window entails a temperature range from 1050 to 1150 °C, a strain rate of 0.01 s^{-1}, and a deformation degree falling between 40% and 60%.

CRediT authorship contribution statement

Shi-qi GUO: Investigation, Writing – Original draft, Formal analysis, Validation, Visualization; **Liang HUANG:** Conceptualization, Writing – Review & editing, Supervision, Project administration, Funding acquisition; **Chang-min LI:** Writing – Modifying, Investigation; **Heng-jun LUO:** Methodology; **Wei XIANG:** Investigation; **Jian-jun LI:** Conceptualization, Supervision, Writing – Review & editing.

Declaration of competing interest

The authors declare that they have no known competing financial interests or personal relationships that could have appeared to influence the work reported in this paper.

Acknowledgments

This work was supported by the National Key Research and Development Program of China (Nos. 2022YFB3706901, 2022YFB3706903) and the National Natural Science Foundation of China (No. 52274382).

References

[1] LI Chang-min, HUANG Liang, ZHAO Ming-jie, GUO Shi-qi, SU Yang, LI Jian-jun. Characterization of hot workability of Ti−6Cr−5Mo−5V−4Al alloy based on hot processing map and microstructure evolution [J]. Journal of Alloys and Compounds, 2022, 905: 164161.

[2] HUANG Liang, LI Chang-min, LI Cheng-lin, HUI Song-xiao, YU Yang, ZHAO Ming-jie, GUO Shi-qi, LI Jian-jun. Research progress on microstructure evolution and hot processing maps of high strength β titanium alloys during hot deformation [J]. Transactions of Nonferrous Metals Society of China, 2022, 32: 3835−3859.

[3] LI Kai, YANG Ping. Strain-induced α-to-β phase transformation during hot compression in Ti−5Al−5Mo−5V−1Cr−1Fe alloy [J]. Transactions of Nonferrous Metals Society of China, 2019, 29: 296−304.

[4] LIAN Qi-hao, ZHANG Chang-jiang, FENG Hong, YANG Zhen-bo, ZHANG Shu-zhi, HAN Jian-chao, WANG Tao, PENG Fan, CAO Peng. Hot deformation temperature and pre-deformation effect on silicide precipitation behavior of (TiB+Y_2O_3)/near α-Ti matrix composite [J]. Transactions of Nonferrous Metals Society of China, 2023, 33: 2660−2671.

[5] NIU Li-qun, ZHANG Qi, WANG Bo, HAN Bin, LI Hao, MEI Tang-jie. A modified Hansel−Spittel constitutive equation of Ti−6Al−4V during cogging process [J]. Journal

of Alloys and Compounds, 2022, 894: 162387.

[6] VOYEVODIN V, TIKHONOVSKY M, ROSTOVA H, KALCHENKO A, KOLODIY I, ANDRIEVSKAYA N, OKOVIT V, SERRANO M, HERNANDEZ R, VELIKODNYI O, LEVENETS A. A new approach to thermo-mechanical treatment of steel T91 by multiple upsetting-extrusion in a ferritic range [J]. Materials Science and Engineering A, 2021, 822: 141686.

[7] WANG Xiang-dong, PAN Qing-lin, LIU Li-li, XIONG Shang-wu, WANG Wei-yi, LAI Jian-ping, SUN Yuan-wei, HUANG Zhi-qi. Characterization of hot extrusion and heat treatment on mechanical properties in a spray formed ultra-high strength Al−Zn−Mg−Cu alloy [J]. Materials Characterization, 2018, 144: 131−140.

[8] QIAN Dong-sheng, LIU Yi, REN Hai-chao, WANG Feng, WU Min, DENG Song. Microstructure and mechanical properties evolution of aviation M50 steel fabricated by the multiple electro-assisted rolling [J]. Journal of Materials Research and Technology, 2022, 20: 496−507.

[9] YANG Zhong-yuan, LIU Hao-wei, CUI Zhen-shan, ZHANG Hai-ming, CHEN Fei. Refinement mechanism of centimeter-grade coarse grains in as-cast Ti2AlNb-based alloy during multi-directional forging [J]. Materials & Design, 2023, 225: 111508.

[10] WANG Lei, LI Wei, JIN Pei-peng, WANG Jin-hui, REN Qian-long, ZHU Lin. Revealing hot deformation behavior and optimizing process parameters of as-cast Ti−5Al−5Mo−5V−1Cr−1Fe alloy [J]. Journal of Materials Research and Technology, 2023, 23: 3602−3616.

[11] XU Wen-xin, ZHAO Zhang-long, WANG Yi-bo, LIU Na, LI Sen, HUANG Xing-yu. Correlation between the strain rate sensitivity exponent m and microstructure evolution during hot deformation of an as-cast TiAl alloy [J]. Materials Characterization, 2023, 203: 113050.

[12] YU Guo-xiang, ZHAO Ding-xuan, LI Keer, CHEN Wei, ZHANG Jin-yu, LIU Ji-xiong, LI Rui, WANG Xiao-xiang, SUN Jun. Homogeneous α-precipitation and enhanced plasticity in Ti−6Cr−5Mo−5V−4Al high-strength metastable titanium alloy with heterogenous β-structure [J]. Materials Science and Engineering A, 2022, 858: 144180.

[13] ZHOU Wei, WANG Chang, LIU Ji-xiong, LI Si-yun, LIU Hui-qun. Ageing precipitation sequence and effect of ω and secondary α phases on tensile properties of metastable β Ti−6Cr−5Mo−5V−4Al alloy [J]. Transactions of Nonferrous Metals Society of China, 2023, 33: 1742−1754.

[14] LI Chang-min, HUANG Liang, ZHAO Ming-jie, GUO Shi-qi, LI Jian-jun. Study on microstructure evolution and deformation mechanism of Ti-6554 based on power dissipation efficiency at supertransus temperatures [J]. Journal of Alloys and Compounds, 2022, 924: 166481.

[15] LI Chang-min, HUANG Liang, ZHAO Ming-jie, GUO Shi-qi, SU Yang, LI Jian-jun. Systematic analysis of the softening mechanism and texture evolution of Ti−6Cr−5Mo−5V−4Al alloy during hot compression in α+β phase region [J]. Materials Science and Engineering A, 2022, 850: 143571.

[16] LONG Shuai, XIA Yu-feng, WANG Peng, ZHOU Yu-ting, GONG-YE Fan-jiao, ZHOU Jie, ZHANG Jian-sheng, CUI Ming-liang. Constitutive modelling, dynamic globularization behavior and processing map for Ti−6Cr−5Mo−5V−4Al alloy during hot deformation [J]. Journal of Alloys and Compounds, 2019, 796: 65−76.

[17] LI Chang-min, HUANG Liang, ZHAO Ming-jie, GUO Shi-qi, LI Jian-jun. Hot deformation behavior and mechanism of a new metastable β titanium alloy Ti−6Cr−5Mo−5V−4Al in single phase region [J]. Materials Science and Engineering A, 2021, 814: 141231.

[18] ZHAO Qin-yang, BOLZONI L, CHEN Yong-nan, XU Yi-ku, TORRENS R, YANG Fei. Processing of metastable beta titanium alloy: Comprehensive study on deformation behaviour and exceptional microstructure variation mechanisms [J]. Journal of Materials Science & Technology, 2022, 126: 22−43.

[19] SHI Shuang-xi, LIU Xiu-sheng, ZHANG Xiao-yong, ZHOU Ke-chao. Comparison of flow behaviors of near beta Ti-55511 alloy during hot compression based on SCA and BPANN models [J]. Transactions of Nonferrous Metals Society of China, 2021, 31: 1665−1679.

[20] LI Chang-min, HUANG Liang, LI Cheng-lin, HUI Song-xiao, YU Yang, ZHAO Ming-jie, GUO Shi-qi, LI Jian-jun. Research progress on hot deformation behavior of high-strength β titanium alloy: Flow behavior and constitutive model [J]. Rare Metals, 2022, 41: 1434−1455.

[21] HUA Ke, ZHANG Yu-dong, GAN Wei-min, KOU Hong-chao, BEAUSIR B, LI Jin-shan, ESLING C. Hot deformation behavior originated from dislocation activity and β to α phase transformation in a metastable β titanium alloy [J]. International Journal of Plasticity, 2019, 119: 200−214.

[22] HUA Ke, WAN Qiong, ZHANG Yong-liang, KOU Hong-chao, ZHANG Fan, LI Jin-shan. Crystallography and microstructure of the deformation bands formed in a metastable β titanium alloy during isothermal compression [J]. Materials Characterization, 2021, 176: 111119.

[23] BAO Jian-xing, LV Shou-dan, ZHANG Mei-wei, SHAN De-bin, GUO Bin, XU Jie. Multi-scale coupling effects on flow localization during micro-compression deformation of Ti−6Al−4V alloy [J]. Materials Science and Engineering A, 2020, 793: 139888.

[24] CHEN Dong, YANG Qian-ru, YANG Na-chuan, WANG Meng, XU Qiang, WU Jing-yuan, JIANG Yan-bin, LI Zhou, XIAO Zhu, WEI Hai-gen. Hot compressive deformation and microstructural evolution of 60NiTi alloy [J]. Transactions of Nonferrous Metals Society of China, 2023, 33: 189−200.

[25] PRASAD Y, GEGEL H, DORAIVELU S. Modeling of dynamic material behavior in hot deformation: Forging of Ti-6242 [J]. Metallurgical and Materials Transactions A, 1984, 15: 1883−1892.

[26] JI Hong-chao, DUAN Hai-long, LI Yao-gang, LI Wang-da, HUANG Xiao-min, PEI Wei-chi, LU Yong-hao. Optimization the working parameters of as-forged 42CrMo steel by constitutive equation-dynamic recrystallization equation and processing maps [J]. Journal of Materials Research and Technology, 2020, 9: 7210−7224.

[27] XU Xin, DONG Li-min, BA Hong-bo, ZHANG Zhi-qiang, YANG Rui. Hot deformation behavior and microstructural evolution of beta C titanium alloy in β phase field [J]. Transactions of Nonferrous Metals Society of China, 2016, 26: 2874−2882.

[28] MURTY S, RAO B. Ziegler's criterion on the instability regions in processing maps [J]. Journal of Materials Science Letters, 1998, 17: 1203−1205.

[29] ZHAO Qin-yang, YANG Fei, TORRENS R, BOLZONI L. Comparison of hot deformation behaviour and microstructural evolution for Ti−5Al−5V−5Mo−3Cr alloys prepared by powder metallurgy and ingot metallurgy approaches [J]. Materials & Design, 2019, 169: 107682.
[30] LIU Qiang, ZHAO Mi-feng, HU Fang-ting, ZHU Guo-chuan, XIE Jun-feng, SONG Sheng-yin, YIN Cheng-xian, YU Yang. Investigation of deformation behavior and microstructure evolution of a Ti−6Al−4V−0.5Ni−0.5Nb−0.05Ru alloy [J]. Materials Characterization, 2021, 173: 110928.
[31] WANG Sheng-long, ZHANG Ming-xian, WU Huan-chun, YANG Bin. Study on the dynamic recrystallization model and mechanism of nuclear grade 316LN austenitic stainless steel [J]. Materials Characterization, 2016, 118: 92−101.
[32] ZENG Rong, HUANG Liang, LI Jian-jun, LI Hong-wei, ZHU Hui, ZHANG Xiao-ting. Quantification of multiple softening processes occurring during multi-stage thermoforming of high-strength steel [J]. International Journal of Plasticity, 2019, 120: 64−87.
[33] GAO Peng-fei, ZHAN Mei, FAN Xiao-guang, LEI Zhen-ni, CAI Yang. Hot deformation behavior and microstructure evolution of TA15 titanium alloy with nonuniform microstructure [J]. Materials Science and Engineering A, 2017, 689: 243−251.
[34] GAO Peng-fei, FU Ming-wang, ZHAN Mei, LEI Zhen-ni, LI Yan-xi. Deformation behavior and microstructure evolution of titanium alloys with lamellar microstructure in hot working process: A review [J]. Journal of Materials Science & Technology, 2020, 39: 56−73.
[35] SOUZA P, HODGSON P, ROLFE B, SINGH R, BELADI H. Effect of initial microstructure and beta phase evolution on dynamic recrystallization behaviour of Ti6Al4V alloy−An EBSD based investigation [J]. Journal of Alloys and Compounds, 2019, 793: 467−479.
[36] CHAUDHURI A, BEHERA A, SARKAR A, KAPOOR R, RAY R, SUWAS S. Hot deformation behaviour of Mo-TZM and understanding the restoration processes involved [J]. Acta Materialia, 2019, 164: 153−164.
[37] YANG Qiu-yue, MA Min, TAN Yuan-biao, XIANG Song, ZHAO Fei, LIANG Yi-long. Microstructure and texture evolution of TB8 titanium alloys during hot compression [J]. Rare Metals, 2021, 40: 2917−2926.
[38] HUANG K, LOGÉ R. A review of dynamic recrystallization phenomena in metallic materials [J]. Materials & Design, 2016, 111: 548−574.
[39] ZHAO Qin-yang, YANG Fei, TORRENS R, BOLZONI L. Evaluation of the hot workability and deformation mechanisms for a metastable beta titanium alloy prepared from powder [J]. Materials Characterization, 2019, 149: 226−238.
[40] SUN Yong-gang, ZHANG Chang-jiang, FENG Hong, ZHANG Shu-zhi, HAN Jian-chao, ZHANG Wang-gang, ZHAO Er-tuan, WANG Hong-wei. Dynamic recrystallization mechanism and improved mechanical properties of a near α high temperature titanium alloy processed by severe plastic deformation [J]. Materials Characterization, 2020, 163: 110281.
[41] CHEN Jia-hao, LI Jin-shan, TANG Bin, CHEN Yi, KOU Hong-chao. Microstructure and texture evolution of a near β titanium alloy Ti-7333 during continuous cooling hot deformation [J]. Progress in Natural Science: Materials International, 2019, 29: 50−56.
[42] ZHAO Juan, ZHONG Jie, YAN Fei, CHAI Fang, DARGUSCH M. Deformation behaviour and mechanisms during hot compression at supertransus temperatures in Ti−10V−2Fe−3Al [J]. Journal of Alloys and Compounds, 2017, 710: 616−627.
[43] QIN Dong-yang, GUO Di-zi, ZHENG Li, LI Yu-long. Dynamic recrystallization of Ti-5553 alloy during sub-transus thermomechanical processing: Mechanisms and its role in formation of a bi-modal structure [J]. Journal of Alloys and Compounds, 2018, 769: 725−731.

铸态 Ti−6Cr−5Mo−5V−4Al 合金毫米级粗晶热加工参数及显微组织演变

郭士琦[1]，黄 亮[1]，李昌民[1,2]，罗恒军[2]，向 伟[2]，李建军[1]

1. 华中科技大学 材料科学与工程学院 材料成形与模具技术全国重点实验室，武汉 430074；
2. 中国第二重型机械集团德阳万航模锻有限责任公司，德阳 618000

摘 要：通过热压缩实验，在温度范围 950~1150 °C、应变速率 0.001~10 s^{-1}、变形程度 20%~80%的条件下，对铸态 Ti−6Cr−5Mo−5V−4Al 合金毫米级粗晶粒(MCGs)的热变形行为和组织演变进行了研究，并建立了热加工图。在压缩方向(RD)，MCGs 内部出现了由亚晶粒渐进旋转引起的连续动态再结晶(CDRX)；而沿横向(TD)，在 MCGs 边界上则产生了由晶界弓出或桥接引起的不连续动态再结晶(DDRX)。随着应变率的降低、温度的升高和变形程度的增加，动态再结晶更加活跃，显著减小了原始平均晶粒尺寸。因此，合理的加工温度范围为 1050~1150 °C、应变速率为 0.01 s^{-1}、变形程度为 40%~60%。

关键词：铸态 Ti-6554 合金；毫米级粗晶粒；变形机制；热加工参数

(Edited by Bing YANG)